ARTICLES
https://doi.org/10.1038/s41563-018-0112-7
nature materials

The relation of local order to material properties in relaxor ferroelectrics

M. J. Krogstad[1,2], P. M. Gehring[3], S. Rosenkranz[1], R. Osborn[1], F. Ye[4], Y. Liu[4], J. P. C. Ruff[5], W. Chen[6], J. M. Wozniak[7,8], H. Luo[9], O. Chmaissem[1,2], Z.-G. Ye[6] and D. Phelan[1]*

Correlating electromechanical and dielectric properties with nanometre-scale order is the defining challenge for the development of piezoelectric oxides. Current lead (Pb)-based relaxor ferroelectrics can serve as model systems with which to unravel these correlations, but the nature of the local order and its relation to material properties remains controversial. Here we employ recent advances in diffuse scattering instrumentation to investigate crystals that span the phase diagram of $PbMg_{1/3}Nb_{2/3}O_3$-$xPbTiO_3$ (PMN-*x*PT) and identify four forms of local order. From the compositional dependence, we resolve the coupling of each form to the dielectric and electromechanical properties observed. We show that relaxor behaviour does not correlate simply with ferroic diffuse scattering; instead, it results from a competition between local antiferroelectric correlations, seeded by chemical short-range order, and local ferroic order. The ferroic diffuse scattering is strongest where piezoelectricity is maximal and displays previously unrecognized modulations caused by anion displacements. Our observations provide new guidelines for evaluating displacive models and hence the piezoelectric properties of environmentally friendly next-generation materials.

The construct of the well ordered crystalline lattice has long provided the foundation for condensed matter science. The concept underlies the description of metals and insulators, of magnets and superconductors, and the structure of matter itself. Deviations from this perfection — disorder and randomness introduced through substitutions and their impact on electronic structure, strain and so on — can drastically modify the behaviours predicted from this simplified model. Such deviations often occur as local ordering phenomena that break long-range, average symmetry at the nanometre scale, but measuring this local order and correlating it with the microscopic physics underlying material behaviour remains a grand challenge. This is epitomized in Pb-based relaxor ferroelectrics — complex perovskite oxides with exceptional electromechanical coupling and large, weakly temperature-dependent dielectric constants that are desirable in numerous applications. Although it is widely agreed that both properties are coupled to locally broken symmetry, the nature of the disordered ground states remains controversial. A frequently employed model consists of nanometre-scale ferroelectric domains, or polar nanoregions[1–5], that are embedded in a non-ferroelectric matrix, and it has been argued that these polar nanoregions strongly influence the dielectric permittivity[6,7] and enhance the electromechanical properties[8–10]. However, this 'raisins-in-the-cake' picture is inconsistent with competing models that instead implicate a large number of low-energy domain walls arising from nanometre-scale variations in the polar displacement vectors[11,12]. Other researchers have highlighted the importance of chemical short-range order[13], competing antiferroelectric and ferroelectric interactions[14], or the contrasting ferroelectric tendencies of different cations occupying crystallographically equivalent sites[15] — all of which influence local atomic displacements and material properties. Pb-based relaxor ferroelectrics thus represent a valuable material with which to test the experimental methodologies that are being developed to determine local order and to correlate order with material performance.

The confusion leading to these different interpretations arises because the relationships between the dielectric and electromechanical properties and the various forms of long-range and especially short-range order have not been well established. These properties vary with composition in the Pb-based relaxor ferroelectric PMN-*x*PT (*x* is in per cent), allowing clarification of these relationships. Figure 1a illustrates the evolution of the average symmetry of single-crystal PMN-*x*PT with composition and temperature[16]. The low-temperature structure transforms from non-ferroelectric, cubic symmetry at $x=0$[17,18] to highly strained ferroelectric, tetragonal symmetry at $x=100$ via two different monoclinic space groups: *Cm* (nearly indistinguishable from rhombohedral *R3m*) and *Pm*. The compositional dependence of the piezoelectric coefficient d_{33}, which relates the strain to an applied electric field, is adapted from ref. [19] and presented in Fig. 1b. Electromechanical properties are poor for both endmembers but anomalously large close to the monoclinic *Pm* phase that borders the tetragonal phase at a morphotropic phase boundary (MPB) near $x \approx 30$. PMN ($x=0$) is generally considered to be a canonical 'relaxor', distinguished by an unusually broad and rounded maximum in dielectric permittivity at a strongly frequency-dependent temperature $T_{max}(\omega)$[5]. The frequency-dependent shift in T_{max}, defined as $\Delta T_{max} = T_{max}(10^6\,\mathrm{Hz}) - T_{max}(10^2\,\mathrm{Hz})$, is approximately 24 K for PMN[20,21]. However, as first elucidated by ref. [21] and reproduced in Fig. 1c, ΔT_{max}, and hence the diffusive characteristics of the material, gradually decreases with *x*. The relaxor characteristics disappear at approximately the composition at which the MPB is reached and the electromechanical response is maximal[22].

[1]Materials Science Division, Argonne National Laboratory, Argonne, IL, USA. [2]Department of Physics, Northern Illinois University, DeKalb, IL, USA. [3]NIST Center for Neutron Research, National Institute of Standards and Technology, Gaithersburg, MD, USA. [4]Neutron Scattering Division, Oak Ridge National Laboratory, Oak Ridge, TN, USA. [5]CHESS, Cornell University, Ithaca, NY, USA. [6]Department of Chemistry and 4D LABS, Simon Fraser University, Burnaby, British Columbia, Canada. [7]Mathematics and Computer Science Division, Argonne National Laboratory, Argonne, IL, USA. [8]Computation Institute, University of Chicago and Argonne National Laboratory, Chicago, IL, USA. [9]Shanghai Institute of Ceramics, Chinese Academy of Sciences, Shanghai, China. *e-mail: dphelan@anl.gov

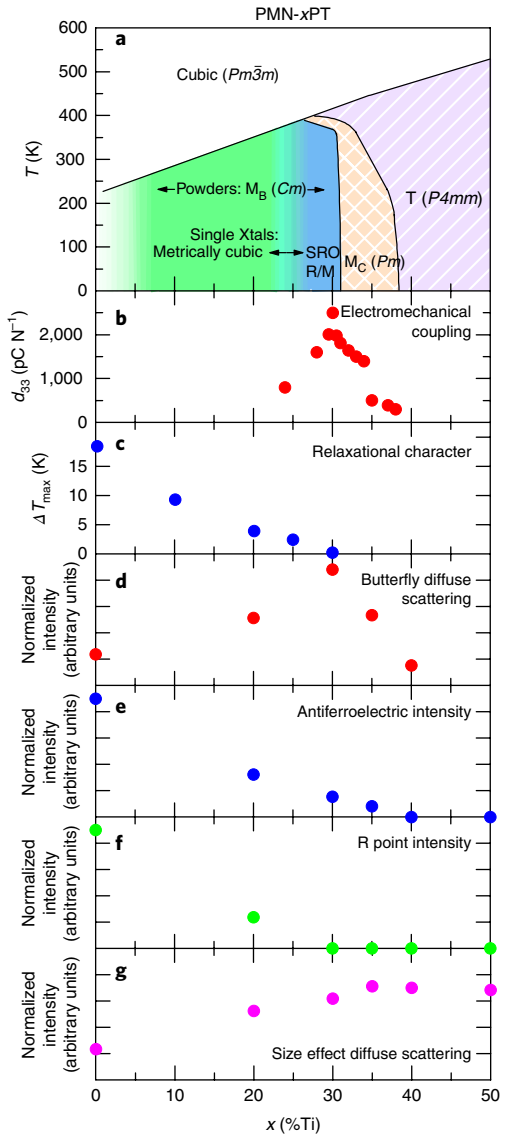

Fig. 1 | Compositional dependence of structure, bulk properties and sources of diffuse scattering of PMN-*x*PT. a, Structural phase diagram for single crystals of PMN-*x*PT as adapted from ref. [16]. 'SRO R/M' refers to a region in the phase diagram where there is short-range rhombohedral or monoclinic order that is resolvable from the splitting of the fundamental Bragg reflections. 'M_c' refers to a monoclinic symmetry with space group *Pm*[50]. 'M_B' refers to a monoclinic symmetry with space group *Cm*[50]. 'T' refers to tetragonal symmetry. 'Single Xtals: metrically cubic' refers to the region in the phase diagram where single crystals are metrically cubic. **b**–**f**, Compositional dependence of various parameters. **b**, The piezoelectric coefficient, d_{33}, as reported for single crystals and adapted from ref. [19]. **c**, ΔT_{max}, as described in the main text. Data were collected and adapted from ref. [21]. **d**, Amplitude of C1 measured with neutrons. Amplitude was estimated by integrating intensity over a section of the diffuse lobes around the 200 Bragg peak, centred on (2.14, 0.14, 0.0). **e**, Amplitude of the M-point scattering (C2), obtained by least-squares fitting of a Gaussian function to the (3.5, 0.5, 0.0) peak. **f**, Amplitude of the R-point scattering (C3) obtained by least-squares fitting of a Gaussian function to the (2.5, 0.5, 0.5) peak. **g**, Amplitude of the size-effect scattering (C4) obtained by integrating over a box of 0.4 × 0.4 × 0.4 reciprocal lattice units (r.l.u.) centred on (3.5, 0, 0). Linear vertical scales are used for **d**–**g**. Data were collected at 6 K for **d**–**g**.

Probing the local order of Pb-based relaxor ferroelectrics. Diffuse neutron and X-ray scattering are classic signatures of local ordering. Both have been well documented in Pb-based relaxor ferroelectrics and characterized as rod-like, centred at Bragg reflections ($\mathbf{q} = \mathbf{Q} - \boldsymbol{\tau}_{Bragg} = 0$, where $\mathbf{q}$ is the reduced wavevector, $\mathbf{Q}$ is the wavevector, and $\boldsymbol{\tau}_{Bragg}$ is the Bragg wavevector), oriented along <110>[3,5,23–25], and resembling 'butterfly'-shaped patterns around the *h*00 peaks. This 'butterfly'-shaped diffuse scattering has been modelled with polar nanoregions[3,25–29], oriented polar domain walls[30], polar correlations between chemically ordered nanoregions[13], Huang scattering[31], thermal-like diffuse scattering[32] or a homogeneous random network of anisotropically coupled dipoles[33]. It has also been associated with ferroic order, relaxor behaviour or both[34,35]; yet there is no consensus on a correct interpretation of the underlying local order or how it influences material properties. Additionally, diffuse scattering centred on the Brillouin zone boundary M points $\frac{1}{2}(2h+1,2k+1,2l)$ has been observed in PMN and attributed to antiferrodistortive displacements of Pb cations[36]. Unusual neutron inelastic scattering from highly damped phonons is observed at these M points and has been associated with antiferroelectric modes[37] that soften to produce broad elastic peaks at low temperature. Diffuse peaks centred on the R points $\frac{1}{2}(2h+1,2k+1,2l+1)$ have also been reported, and have been attributed to ordering of Mg^{2+} and Nb^{5+} ions[36,38].

By employing instrumentation that represents a breakthrough in our ability to measure large, three-dimensional volumes of neutron elastic diffuse scattering efficiently, we identify how the different forms of local order in PMN-*x*PT correlate with the dielectric and electromechanical properties as well as with the long-range ordered polar states. These correlations are unravelled via systematic study of the compositional dependence of the neutron elastic diffuse scattering from a collection of crystals that span the structural phase diagram, with compositions that have been precisely determined via prompt gamma activation analysis. We have performed extensive and complementary neutron and X-ray diffuse scattering measurements, each covering a large three-dimensional volume of reciprocal space and enabling a survey of many Brillouin zones across the whole phase diagram of PMN-*x*PT. By implementing cross-correlation with a pseudorandom chopper, the neutron measurements provide both elastic and energy-integrated signals, allowing us to determine whether the measured diffuse scattering is of static or dynamic origin (see Methods).

These measurements reveal four distinct sources of diffuse scattering, which we refer to as C1 to C4; each evolves uniquely with composition, allowing us to correlate each source with the dielectric and electromechanical properties. This leads to the following findings: (1) The 'butterfly' scattering, which is frequently conflated with both polar nanoregions and relaxors, is not a unique signature of the relaxor state because its intensity does not correlate with the relaxational dielectric behaviour. If it arises from polar nanoregions, its presence alone is insufficient to produce the relaxor state; (2) the 'butterfly' scattering displays previously unrecognized intensity modulations originating from oxygen displacements that render existing models inadequate; (3) short-range antiferroelectricity, probably seeded by local chemical ordering, strongly correlates with relaxational behaviour and must play an important part in its origin; and (4) the 'butterfly' scattering is maximal near the MPB and correlates with electromechanical coupling.

Ferroic diffuse scattering. Broad surveys of the neutron diffuse scattering ($T = 6$ K) in four different pseudocubic scattering planes: $l = 0$, $l = 1$, $l = 2.5$, and $l = 3.5$ are shown in Fig. 2a–d for $x = 0$ and in Fig. 2e–h for $x = 30$. The $l = 0$ and $l = 1$ planes contain the principal Bragg reflections, which in a perfect crystal would appear as delta functions broadened only by the instrumental resolution. However, intense diffuse scattering centred on each zone centre ($\mathbf{q} = 0$) is also present. We refer to this as component 1 (C1) as marked by the red circles in Fig. 2. C1, commonly referred to as 'butterfly' scattering, has received the most attention in previous studies and has

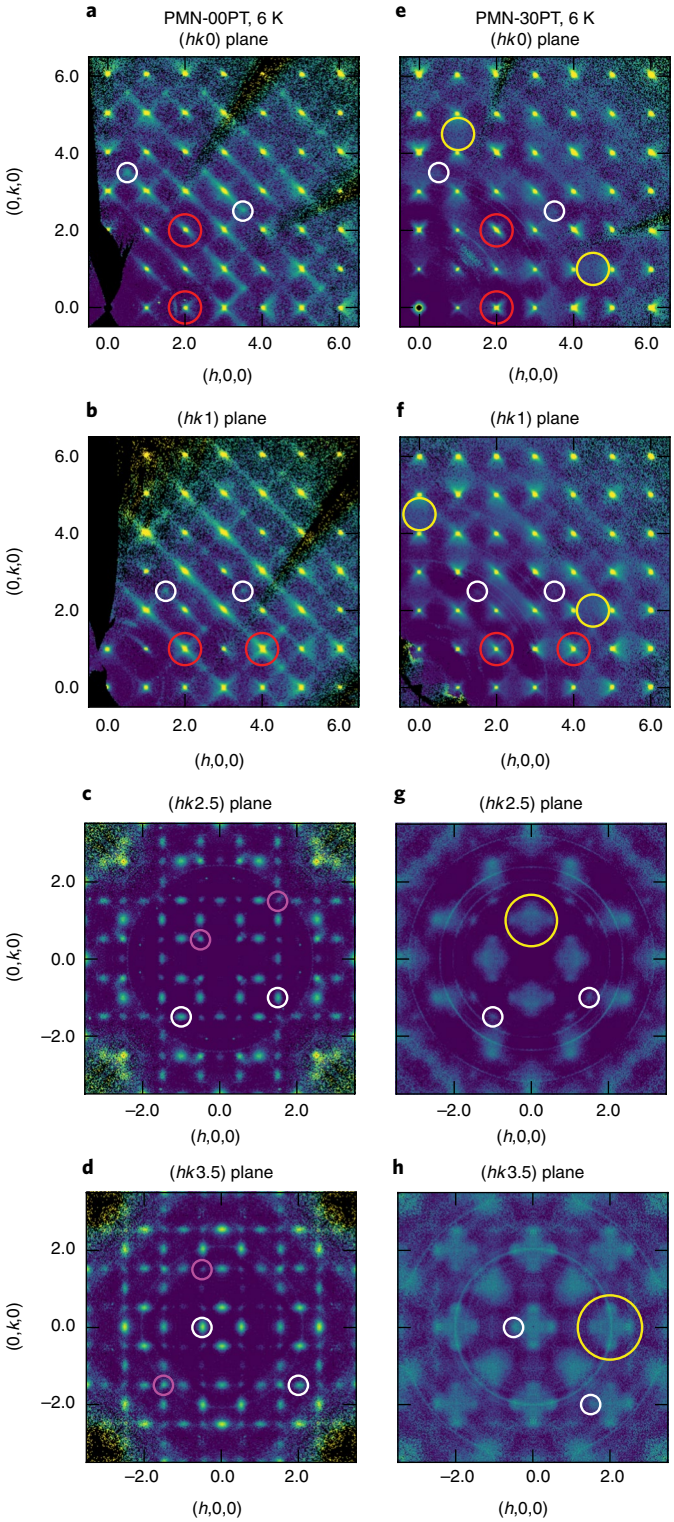

Fig. 2 | Reciprocal space maps of neutron scattering intensities measured on the Corelli instrument at 6 K. Data are shown in the $l = 0$, 1, 2.5 and 3.5 planes in panels **a**, **b**, **c** and **d** for $x = 0$ and in **e**, **f**, **g** and **h** for $x = 30$, respectively. Data have been integrated over a range in l corresponding to the mean value ± 0.03 r.l.u. Four different diffuse scattering features, as discussed in the text, are indicated with coloured circles: C1, red; C2, white; C3, magenta; and C4, yellow. Intensity scales are logarithmic.

a ferroic nature revealed by a marked electric field dependence[39]. Most measurements of C1 have been limited to a small number of mainly low-|**Q**| Brillouin zones because these are the easiest to measure in conventional scattering measurements (such as triple-axis). However, our broad surveys clearly indicate interzone intensity modulations to C1. When the Miller indices *hkl* of a Bragg peak are all odd or all even, then C1 is stronger on the high-|**Q**| side of the Bragg peak; otherwise, the scattering is stronger on the low-|**Q**| side. This holds for all Brillouin zones and is most easily visualized along <*h*00>, where successive zones have diffuse intensities that alternate between strong high-|**Q**| and strong low-|**Q**|.

Most previous neutron studies have focused on a few Brillouin zones and were thus unable to identify this asymmetry[23,24,26,27]. Although it is not surprising that this feature had not been appreciated in previous neutron scattering measurements confined to a small number of Brillouin zones, in retrospect it is recognizable in previous reports on PMN and related systems[23,40–43]. However, it is surprising that this intensity modulation was not reported in synchrotron X-ray studies, which provide access to a much larger **Q** range. We therefore carried out complementary X-ray scattering experiments (Supplementary Fig. 1 shows X-ray scattering intensity maps measured on pieces taken from the same crystals in the same planes as shown for neutrons in Fig. 2). Figure 3 compares the diffuse scattering surrounding 400 for $x = 30$ in the $l = 0$ plane for X-rays (Fig. 3a) and neutrons (Fig. 3d), and it appears that the low-|**Q**| and high-|**Q**| intensities are much closer to equal for X-rays than for neutrons. This is confirmed by examination of the $(3.9, k, l)$ and $(4.1, k, l)$ planes, which illustrate the distribution of C1 on the low-|**Q**| and high-|**Q**| sides of 400, respectively, for both X-rays (Fig. 3b,c) and neutrons (Fig. 3e,f). The large difference in intensity between the low-|**Q**| and high-|**Q**| diffuse lobes measured with neutrons around this peak does not match the nearly equal intensity distribution of the same diffuse lobes measured with X-rays. For peaks of all even or all odd Miller indices, the C1 intensity is close to symmetric when measured with X-rays; for peaks of mixed even and odd indices, we observe the same asymmetry with X-rays as with neutrons with a less extreme difference in intensity.

The large penetration depths of both the neutrons and the high-energy X-rays used in our study (see Methods) ensure that both probes sampled the bulk of the crystals, so the observed difference is not due to a skin effect[16,44,45]. The low-|**Q**|/high-|**Q**| interzone modulations are present in both the elastic and energy-integrated neutron cross-sections, indicating that this difference between neutron and X-ray data is not due to the integration of low-lying phonon modes in the X-ray experiments and that this feature is static in origin. The observed differences are intrinsic and result from differences in diffuse scattering structure factors caused by the disparate scattering lengths of the constituent atoms for these two probes. Whereas the scattering of X-rays is dominated by the heavy Pb cations, neutrons are more sensitive to oxygen anions. Calculations of Bragg structure factors (described in Supplementary Information section II) demonstrate the influence of oxygen in tetragonal, Ti-rich compositions where similar modulations can occur (see Supplementary Fig. 2). We therefore conclude that correlated oxygen displacements play a significant part in C1.

We now consider the compositional dependence of C1. Reciprocal space maps of neutron diffuse scattering for the *h*00 set of Brillouin zones for different compositions are shown in Fig. 4a–e (full maps of the $l = 0$ plane are shown in Supplementary Fig. 3). The compositional dependence of C1 is most easily illustrated by the set of linear cuts offset by $k = 0.14$ r.l.u., as shown in Fig. 4f–j. C1 is clearly present for $0 \leq x \leq 35$. At $x = 40$ the intensity is drastically weaker, and a tetragonal domain structure appears, which causes the *h*00 Bragg peaks to split. Qualitatively, C1 is most rod-like at $x = 0$ and becomes increasingly centralized (pushed in towards $\mathbf{q} = 0$) as x tends towards the MPB (though it still extends out well beyond the Bragg peak). The amplitude of C1, shown in Fig. 1d, increases with x from $x = 0$ to $x = 30$, where it is maximal; it then falls off precipitously upon further increase in x. (See Supplementary Information

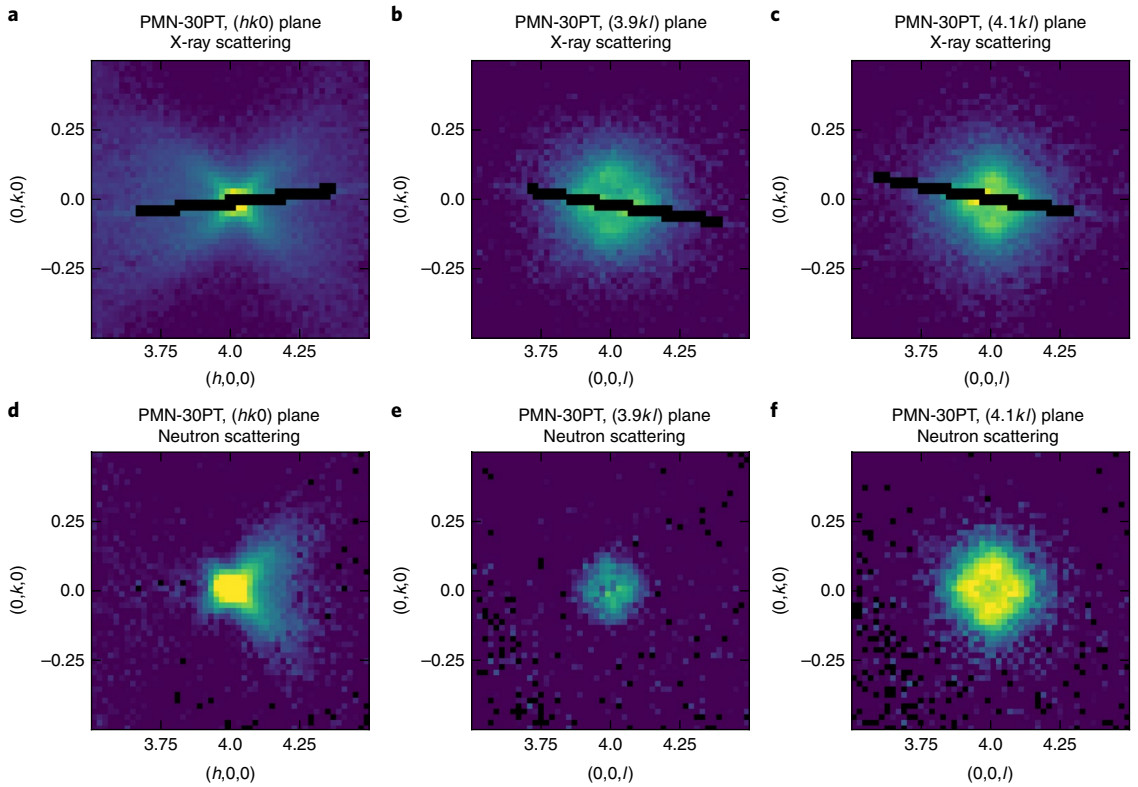

Fig. 3 | Comparison of X-ray and neutron diffuse scattering. Diffuse scattering patterns in the 400 Brillouin zone are shown for $x = 30$. **a**–**c**, $(h, k, 0)$, $(3.9, k, l)$ and $(4.1, k, l)$ planes measured at 100 K with X-rays. **d**–**f**, $(h, k, 0)$, $(3.9, k, l)$ and $(4.1, k, l)$ planes measured at 6 K with neutrons. The $(3.9, k, l)$ and $(4.1, k, l)$ planes show the lobes of scattering in the planes perpendicular to the $(h, k, 0)$ plane as marked in panels **a** and **d**. Data have been integrated in the normal direction over a range of ± 0.01 r.l.u. from the mean value. Intensity scales are logarithmic. Black bars in **a**–**c** indicate regions where reliable data were not collected.

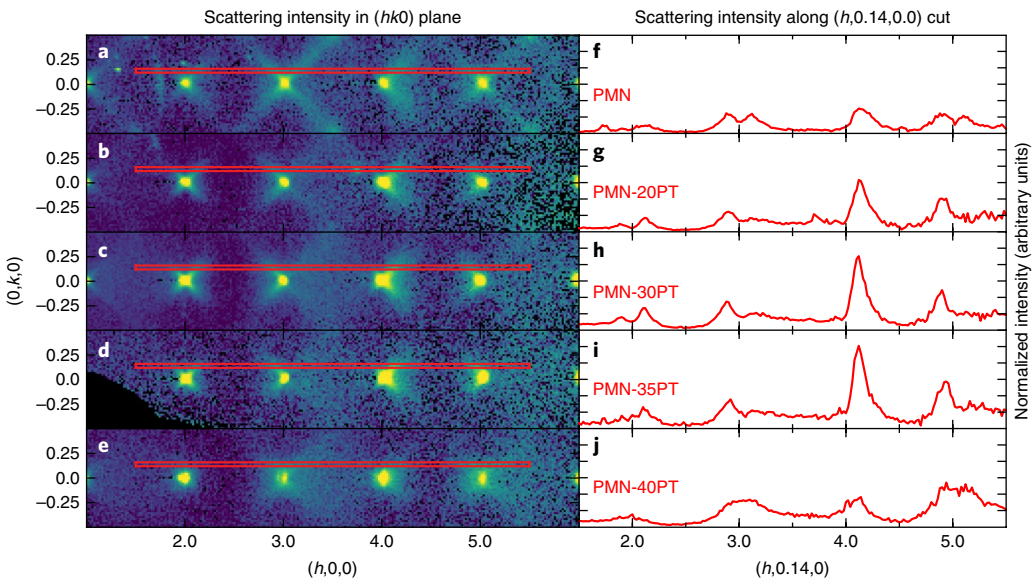

Fig. 4 | Compositional dependence of 'butterfly' diffuse scattering. a–**e**, Reciprocal space maps of the $h00$ set of Brillouin zones in the $(hk0)$ plane measured at 6 K with neutrons are shown for $x = 0$, 20, 30, 35 and 40 respectively, integrated over a range of -0.03 to 0.03 r.l.u. in l. Intensity scales are logarithmic. **f**–**j**, Corresponding cuts through the data in **a**–**e** along $(h, 0.14, 0)$ with intensities integrated along k from 0.11 to 0.17 r.l.u. and along l from −0.03 to 0.03 r.l.u. Vertical scales are linear.

section III and Supplementary Fig. 4 for details of the calculation of its $\mathbf{q}$ dependence.) The enhancement of the $\mathbf{q} = 0$ component upon increasing x towards the MPB is consistent with ref.[46], and the disappearance of C1 in the tetragonal phase is consistent with the finding of a lack of diffuse scattering for $x = 60$ (ref. [43]). Thus, C1 is present in all compositions on the Ti-poor side of the MPB, and its amplitude peaks in the *Pm* phase that forms the MPB but disappears on the Ti-rich side of the MPB.

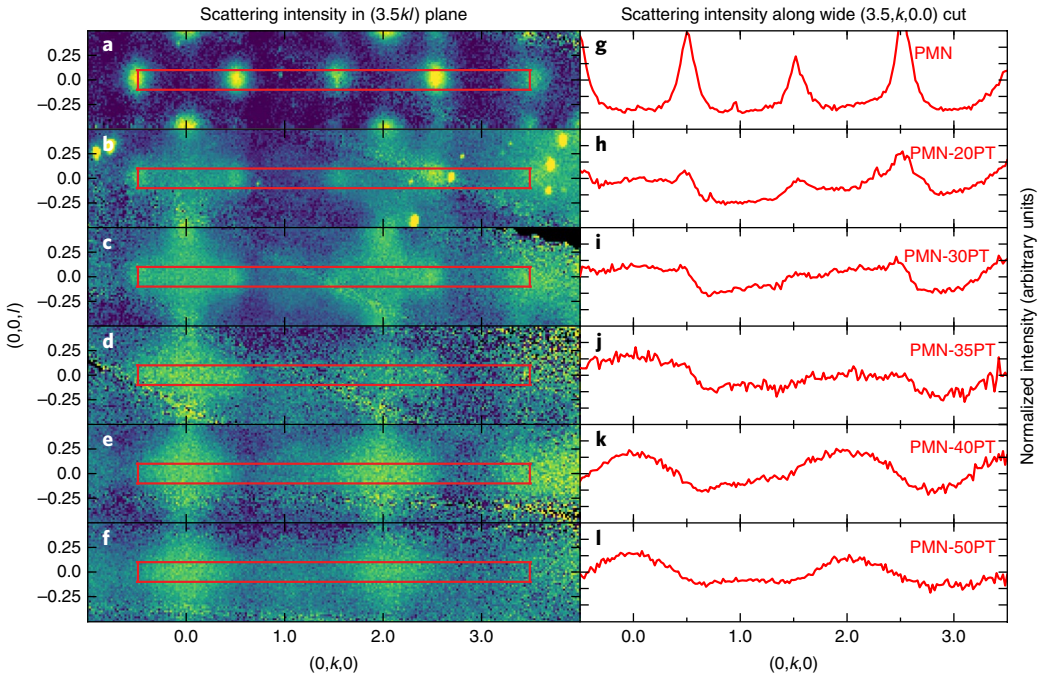

Fig. 5 | Compositional dependence of zone boundary diffuse scattering. a–f, Reciprocal space maps of the (3.5*kl*) plane measured at 6 K with neutrons for $x = 0$, 20, 30, 35, 40 and 50, respectively, integrated over a range of 3.39 to 3.61 r.l.u. in *h*. Intensity scales are logarithmic. **g–l**, Corresponding cuts through the data in **a–f** along (3.5, *k*, 0), with intensities integrated in *h* from 3.39 to 3.61 r.l.u. and in *l* from −0.11 to 0.11 r.l.u. Vertical scales are linear. Points from PMN-20PT that were dominated by a misaligned crystallite were removed.

Despite significant discussion in the literature relating C1 diffuse scattering to relaxor physics, a comparison of the compositional dependence of ΔT_{max} (Fig. 1c) to that of C1 (Fig. 1d) shows that C1 is maximal where the relaxational character is essentially absent. This indicates that C1 is not directly related to relaxational dielectric behaviour. However, it is notable that both d_{33} and C1 are maximal at the MPB ($x \approx 30$). This suggests a physical connection between the electromechanical coupling and C1. That said, C1 is also present in compositions (such as $x = 0$, 20) for which electromechanical properties are poor, so its presence alone cannot account for electromechanical coupling. Strong electromechanical coupling implies a free-energy landscape in which multiple states have similar energies such that their populations are influenced by external electric fields. Such a situation would lead to competing mesoscopic domains that are enhanced at the MPB and thus enhance C1. Adaptive phase models[47] and anomalous domain wall densities[11] have been considered as potential mechanisms that could connect electromechanical coupling to C1. Our measurements highlight the need to account for oxygen displacements in modelling and understanding strong electromechanical coupling in this system.

Diffuse scattering around zone boundaries. A second contribution to the diffuse scattering, C2, forms broad peaks centred on zone-boundary M points. These are apparent in Fig. 2 for $x = 0$ (indicated by white circles), but are strongly suppressed for $x = 30$. As mentioned above, M-point scattering has been reported in X-ray scattering experiments for crystals with $x = 0$ (refs [36,48]) and $x = 6$ (ref. [36]), but it was unresolvable for $x = 10$ (ref. [36]). These peaks have been attributed to antiferrodistortive Pb displacements[36], and neutron inelastic scattering experiments have shown that they originate from the condensation of unusually damped, soft optic phonons[37]. In Fig. 5a–f, we show neutron scattering contours in the $h = 3.5$ plane for all compositions, and cuts (Fig. 5g–j) are made through the scattering contours to illustrate how the amplitude of the M point changes with composition. It is apparent that the M points are strongest for $x = 0$, diminish in amplitude with increasing x, and are essentially absent at the MPB. This compositional dependence is displayed in Fig. 1e, and a comparison with ΔT_{max} (Fig. 1c) shows a clear correlation between the relaxational character and the M-point intensity. The C2 compositional dependence thus strongly suggests a link between short-range antiferroelectric displacements and relaxor physics. Whereas C1 is ferroic, C2 is antiferroelectric in origin[37]. We suggest that the compositional dependence revealed from our work supports a picture in which relaxor physics arises from competing ferroelectric and antiferroelectric interactions[36]. Indeed, this idea is consistent with recent theoretical work[14] describing the relaxor state as a soft pseudospin glass resulting from frustration between competing ferroelectric and antiferroelectric interactions. In this picture, which may extend to relaxor systems beyond PMN-*x*PT such as BZT[15], the ferroic interactions leading to C1 are inhibited by the antiferroelectric interactions underlying C2.

Another component of the diffuse scattering, C3, is observed at the zone-boundary R points. This feature is composed of broad peaks similar to C2, but the peaks at the R points have a distinct temperature dependence. The temperature dependence for all C3 peaks is not identical; for example, the (3.5, 0.5, 0.5) peak is suppressed at higher temperatures, while the (2.5, 0.5, 0.5) peak retains most of its intensity up to 700 K. This suggests two contributions to C3: a temperature-dependent part of similar origin to C2 and a temperature-independent part of chemical origin (see Supplementary Fig. S5 and discussion in Supplementary Information section IV). The temperature-independent scattering, similar to scattering originally revealed in transmission electron microscopy studies[38] and later seen in X-ray measurements[36,48] almost certainly arises from ordering of B-site cations. Although it is too broad to be produced by highly ordered large domains, this scattering indicates short-range rock-salt ordering, with nearest-neighbour pairs of Mg–Mg atoms less likely to occur than would be expected from a random distribution. Our neutron measurements show that this ordering diminishes with increasing x (Fig. 1f), consistent with

the transmission electron microscopy[38] findings. Clearly, the B-site (2+/5+) ordering occurs to minimize the local Coulomb energy, as it is impossible for this order to persist over long distances in PMN-*x*PT and maintain charge neutrality. As Ti^{4+} ions are introduced with increasing *x*, the propensity for charge ordering diminishes. Ref. [13] has discussed the importance of chemical short-range order in seeding locally polar regions in $PbSc_{1/2}Nb_{1/2}O_3$; however, while there is certainly a correlation between the local cation ordering (shown in Fig. 1f) and the relaxational dielectric behaviour (Fig. 1c), there is no obvious correlation to the polar nanoregions, which are often associated with C1 (Fig. 1d). Recent theoretical work suggests that local cation ordering is associated with increased antiferroelectric activity[49]. While this may explain the correspondence of C2 and C3 intensities, it is important to note the absence of C3 intensity near the MPB. Our data indicate that where ferroic properties are maximal, B-site cations are randomly distributed, and a highly ordered arrangement of these atoms cannot be responsible for the ferroic properties in PMN-*x*PT.

A fourth diffuse scattering component, C4, was also observed via neutrons and X-rays. It appears as extremely broad scattering that has a pseudo-octahedral shape centred at X points $\frac{1}{2}(2h+1, 2k, 2l)$ as marked by the yellow circles in Fig. 2. The compositional dependence is apparent from the broad humps centred at the X points in the cuts shown in, for example, Fig. 5j, and the compositional dependence is displayed in Fig. 1g. C4 is modulated across Brillouin zones, with strong and weak octahedra forming a checkerboard pattern in reciprocal space. C4 exists for all compositions measured; it grows initially upon increasing *x* and is thus not directly correlated to the dielectric properties, electromechanical coupling or the long-range polar order. It is reminiscent of diffuse scattering in binary alloys due to atomic size mismatch, suggesting that differences between the average Pb–Mg, Pb–Nb and Pb–Ti nearest-neighbour distances produce this feature. A simple model that displaces Pb cations away from Nb^{5+} cations and towards both Mg^{2+} and Ti^{4+} cations replicates the observed pattern of diffuse octahedra of C4 (Supplementary Fig. 6 and description in Supplementary Information section V), indicating that Pb displacements are correlated to B-site neighbours. C4 can lead to confusion when interpreting diffuse scattering within a single Brillouin zone.

Outlook. Four distinct types of diffuse scattering in PMN-*x*PT are now identified and correlated with the electromechanical and dielectric properties. The ferroic diffuse scattering (C1) exhibits a structure that varies strongly between Brillouin zones and requires consideration of both cation and oxygen displacements. Existing models of C1 must be re-evaluated, because it is now clear that reproducing the diffuse scattering in only one or two Brillouin zones, or by considering only one cation, is insufficient to judge the validity of a model. The correlation of C1 with electromechanical coupling may be understood as resulting from competing ferroic domain states near the MPB. This suggests that the search for Pb-free electromechanical materials should focus on materials that have such competing ferroic domain states. Attribution of relaxor behaviour and physics solely to the ferroic order that gives rise to C1 is inadequate. Our study suggests a picture of relaxors in which competition between local ferroelectric and antiferroelectric correlations leads to relaxational dielectric properties in Pb-based oxides owing to frustration. As chemical ordering and antiferroelectric correlations are reduced, relaxational properties dissipate; this mechanism should be explored in other relaxor systems.

Methods

Methods, including statements of data availability and any associated accession codes and references, are available at https://doi.org/10.1038/s41563-018-0112-7.

Received: 28 July 2017; Accepted: 22 May 2018;
Published online: 25 June 2018

References

1. Burns, G. & Dacol, F. H. Glassy polarization behavior in ferroelectric compounds $Pb(Mg_{1/3}Nb_{2/3})O_3$ and $Pb(Zn_{1/3}Nb_{2/3})O_3$. *Solid State Commun.* **48**, 853–856 (1983).
2. Xu, G. Probing local polar structures in PZN-xPT and PMN-xPT relaxor ferroelectrics with neutron and x-ray scattering. *J. Phys. Conf. Ser.* **320**, 012081 (2011).
3. Gehring, P. M. Neutron diffuse scattering in lead-based relaxor ferroelectrics and its relationship to the ultra-high piezoelectricity. *J. Adv. Dielectr.* **2**, 1241005 (2012).
4. Westphal, V., Kleeman, W. & Glinchuk, M. D. Diffuse phase transitions and random-field-induced domain states of the 'relaxor' ferroelectric $PbMg_{1/3}Nb_{2/3}O_3$. *Phys. Rev. Lett.* **68**, 847–850 (1992).
5. Cowley, R. A., Gvasaliya, S. N., Lushnikov, S. G., Roessli, B. & Rotaru, G. M. Relaxing with relaxors: a review of relaxor ferroelectrics. *Adv. Phys.* **60**, 229–327 (2011).
6. Fu, D. et al. Relaxor $Pb(Mg_{1/3}Nb_{2/3})O_3$: a ferroelectric with multiple inhomogeneities. *Phys. Rev. Lett.* **103**, 207601 (2009).
7. Ni, Y., Chen, H. T., Shi, Y. P., He, L. H. & Soh, A. K. Modeling of polar nanoregions dynamics on the dielectric response of relaxors. *J. Appl. Phys.* **113**, 224104 (2013).
8. Li, F. et al. The origin of ultrahigh piezoelectricity in relaxor-ferroelectric solid solution crystals. *Nat. Commun.* **7**, 13807 (2016).
9. Li, F., Xu, Z. & Zhang, S. The effect of polar nanoregions on electromechanical properties of relaxor-PbTiO3 crystals: extracting from electric-field-induced polarization and strain behaviors. *Appl. Phys. Lett.* **105**, 122904 (2014).
10. Pirc, R., Blinc, R. & Vikhnin, V. S. Effect of polar nanoregions on giant electrostriction and piezoelectricity in relaxor ferroelectrics. *Phys. Rev. B* **69**, 212105 (2004).
11. Takenaka, H., Grinberg, I., Liu, S. & Rappe, A. M. Slush-like polar structures in single-crystal relaxors. *Nature* **546**, 391–395 (2017).
12. Hlinka, J. Do we need the ether of polar nanoregions? *J. Adv. Dielectr.* **2**, 1241006 (2012).
13. Burton, B. P., Cockayne, E. & Waghmare, U. V. Correlations between nanoscale chemical and polar order in relaxor ferroelectrics and the lengthscale for polar nanoregions. *Phys. Rev. B* **72**, 064113 (2005).
14. Sherrington, D. BZT: a soft pseudospin glass. *Phys. Rev. Lett.* **111**, 227601 (2013).
15. Akbarzadeh, A. R., Prosandeev, S., Walter, E. J., Al-Barakaty, A. & Bellaiche, L. Finite-temperature properties of $Ba(Zr,Ti)O_3$ relaxors from first principles. *Phys. Rev. Lett.* **108**, 257601 (2012).
16. Phelan, D. et al. Phase diagram of the relaxor ferroelectric (1−x) $Pb(Mg_{1/3}Nb_{2/3})O_3$-$xPbTiO_3$ revisited: a neutron powder diffraction study of the relaxor skin effect. *Phase Transit.* **88**, 283–305 (2015).
17. Bonneau, P. et al. X-ray and neutron diffraction studies of the diffuse phase transition in ceramics. *J. Solid State Chem.* **91**, 350–361 (1991).
18. de Mathan, N. et al. A structural model for the relaxor $PbMg_{1/3}Nb_{2/3}O_3$ at 5 K. *J. Phys. Condens. Matter* **3**, 8159–8171 (1991).
19. Guo, Y. et al. The phase transition sequence and the location of the morphotropic phase boundary region in (1− x)$[Pb(Mg_{1/3}Nb_{2/3})O_3]$–$xPbTiO_3$ single crystal. *J. Phys. Condens. Matter* **15**, L77 (2003).
20. Bokov, A. A. & Ye, Z. G. Recent progress in relaxor ferroelectrics with perovskite structure. *J. Mater. Sci.* **41**, 31–52 (2006).
21. Grinberg, I., Juhás, P., Davies, P. & Rappe, A. Relationship between local structure and relaxor behavior in perovskite oxides. *Phys. Rev. Lett.* **99**, 267603 (2007).
22. Kutnjak, Z., Petzelt, J. & Blinc, R. The giant electromechanical response in ferroelectric relaxors as a critical phenomenon. *Nature* **441**, 956–959 (2006).
23. Goossens, D. J. Diffuse scattering from lead-containing ferroelectric perovskite oxides. *ISRN Mater. Sci.* **2013**, 107178 (2013).
24. Goossens, D. J. Local ordering in lead-based relaxor ferroelectrics. *Acc. Chem. Res.* **46**, 2597–2606 (2013).
25. Xu, G., Zhong, Z., Hiraka, H. & Shirane, G. Three-dimensional mapping of diffuse scattering in $Pb(Zn_{1/3}Nb_{2/3})O_3$-$xPbTiO_3$. *Phys. Rev. B* **70**, 174109 (2004).
26. Xu, G., Shirane, G., Copley, J. R. D. & Gehring, P. M. Neutron elastic diffuse scattering study of $Pb(Mg_{1/3}Nb_{2/3})O_3$. *Phys. Rev. B* **69**, 064112 (2004).
27. Hiraka, H., Lee, S.-H., Gehring, P. M., Xu, G. & Shirane, G. Cold neutron study on the diffuse scattering and phonon excitations in the relaxor $Pb(Mg_{1/3}Nb_{2/3})O_3$. *Phys. Rev. B* **70**, 184105 (2004).
28. Gehring, P. M. et al. Reassessment of the Burns temperature and its relationship to the diffuse scattering, lattice dynamics, and thermal expansion in relaxor $Pb(Mg_{1/3}Nb_{2/3})O_3$. *Phys. Rev. B* **79**, 224109 (2009).

29. Stock, C. et al. Universal static and dynamic properties of the structural transition in $Pb(Zn_{1/3}Nb_{2/3})O_3$. *Phys. Rev. B* **69**, 094104 (2004).
30. Paściak, M., Wołcyrz, M. & Pietraszko, A. Interpretation of the diffuse scattering in Pb-based relaxor ferroelectrics in terms of three-dimensional nanodomains of the <110>-directed relative interdomain atomic shifts. *Phys. Rev. B* **76**, 014117 (2007).
31. Vakhrushev, S., Ivanov, A. & Kulda, J. Diffuse neutron scattering in relaxor ferroelectric $PbMg_{1/3}Nb_{2/3}O_3$. *Phys. Chem. Chem. Phys.* **7**, 2340 (2005).
32. Bosak, A., Chernyshov, D., Vakhrushev, S. & Krisch, M. Diffuse scattering in relaxor ferroelectrics: true three-dimensional mapping, experimental artefacts and modelling. *Acta Crystallogr. A.* **68**, 117–123 (2012).
33. Takenaka, H., Grinberg, I. & Rappe, A. M. Anisotropic local correlations and dynamics in a relaxor ferroelectric. *Phys. Rev. Lett.* **110**, 147602 (2013).
34. Phelan, D. et al. Role of random electric fields in relaxors. *Proc. Natl Acad. Sci. USA* **111**, 1754 (2014).
35. Stock, C. et al. Neutron and x-ray diffraction study of cubic [111] field-cooled $Pb(Mg_{1/3}Nb_{2/3})O_3$. *Phys. Rev. B* **76**, 064122 (2007).
36. Tkachuk, A. & Chen, H. Anti-ferrodistortive nanodomains in PMN relaxor. *AIP Conf. Proc.* **677**, 55 (2003).
37. Swainson, I. et al. Soft phonon columns on the edge of the Brillouin zone in the relaxor $PbMg_{1/3}Nb_{2/3}O_3$. *Phys. Rev. B* **79**, 224301 (2009).
38. Hilton, A. D., Barber, D. J., Randall, C. A. & Shrout, T. R. On short range ordering in the perovskite lead magnesium niobate. *J. Mater. Sci.* **25**, 3461–3466 (1990).
39. Xu, G., Zhong, Z., Bing, Y., Ye, Z.-G. & Shirane, G. Electric-field-induced redistribution of polar nano-regions in a relaxor ferroelectric. *Nat. Mater.* **5**, 134–140 (2006).
40. Li, Q. *et al.* Soft phonon modes and diffuse scattering in $Pb(In_{1/2}Nb_{1/2})O_3$-$Pb(Mg_{1/3}Nb_{2/3})O_3$-$PbTiO_3$ relaxor. Preprint at https://arxiv.org/abs/1610.09768 (2016).
41. Pasciak, M. et al. Assessing local structure in $PbZn_{1/3}Nb_{2/3}O_3$ using diffuse scattering and reverse Monte Carlo refinement. *Metall. Mater. Trans. A* **44**, 87–93 (2013).
42. Welberry, T. R. et al. Single-crystal neutron diffuse scattering and Monte Carlo study of the relaxor ferroelectric $PbZn_{1/3}Nb_{2/3}O_3$ (PZN). *J. Appl. Crystallogr.* **38**, 639–647 (2005).
43. Stock, C. et al. Damped soft phonons and diffuse scattering in $40\%Pb(Mg_{1/3}Nb_{2/3})O_3$-$60\%PbTiO_3$. *Phys. Rev. B* **73**, 064107 (2006).
44. Xu, G., Viehland, D., Li, J. F., Gehring, P. M. & Shirane, G. Evidence of decoupled lattice distortion and ferroelectric polarization in the relaxor system PMN-*x*PT. *Phys. Rev. B* **68**, 212410 (2003).
45. Gehring, P. M., Chen, W., Ye, Z.-G. & Shirane, G. The non-rhombohedral low-temperature structure of PMN-10% PT. *J. Phys. Condens. Matter* **16**, 7113 (2004).
46. Matsuura, M. et al. Composition dependence of the diffuse scattering in the relaxor ferroelectric compound $(1-x)Pb(Mg_{1/3}Nb_{2/3})O_3$–$xPbTiO_3$ ($0 \leq x \leq 0.40$). *Phys. Rev. B* **74**, 144107 (2006).
47. Jin, Y. M., Wang, Y. U. & Khachaturyan, A. G. Conformal miniaturization of domains with low domain-wall energy: monoclinic ferroelectric states near the morphotropic phase boundaries. *Phys. Rev. Lett.* **91**, 197601 (2003).
48. Vakhrushev, S., Nabereznov, A., Sinha, S. K., Feng, Y. P. & Egami, T. Synchrotron X-ray scattering study of lead magnoniobate relaxor ferroelectric crystals. *J. Phys. Chem. Solids* **57**, 1517–1523 (1996).
49. Prosandeev, S. & Bellaiche, L. Effects of atomic short-range order on properties of the $PbMg_{1/3}Nb_{2/3}O_3$ relaxor ferroelectric. *Phys. Rev. B* **94**, 180102 (2016). (R).

Acknowledgements

Work at the Materials Science Division at Argonne National Laboratory was supported by the US Department of Energy, Office of Science, Materials Sciences and Engineering Division. Research conducted at ORNL's Spallation Neutron Source was sponsored by the Scientific User Facilities Division, Office of Basic Energy Sciences, US Department of Energy. Research conducted at the Cornell High Energy Synchrotron Source (CHESS) was supported by the NSF and NIH/NIGMS via NSF award DMR-1332208. The work at Simon Fraser University was supported by the US Office of Naval Research (ONR grant numbers N00014-12-11045 and N00014-16-1-3106) and the Natural Sciences and Engineering Research Council of Canada (NSERC grant number 203773). We acknowledge the support of the National Institute of Standards and Technology, US Department of Commerce, in providng access to the neutron Prompt Gamma Activation Analysis (PGAA) research facilities used in this work. We also acknowledge the assistance of R. Paul in performing the PGAA measurements and data analysis.

Author Contributions

D.P. directed the project with guidance from P.M.G. M.J.K., P.M.G., S.R., F.Y., Y.L. and D.P. performed the diffuse neutron scattering experiments. M.J.K., S.R., J.P.C.R., R.O. and D.P. performed the X-ray diffuse scattering experiments. J.M.W. and R.O. developed the infrastructure to transform X-ray data into reciprocal space. W. Chen, Z.-G.Y. and H.L. grew single crystals. P.M.G. performed neutron prompt gamma measurements and analysis. M.J.K. performed the diffuse scattering analysis. D.P., M.J.K., P.M.G. and S.R. wrote the manuscript, with contributions from R.O., Z.-G.Y., Y.L., F.Y. and J.P.C.R. O.C. provided guidance to M.J.K.

Competing Interests

The authors declare no competing interests.

Additional information

Supplementary information is available for this paper at https://doi.org/10.1038/s41563-018-0112-7.

Reprints and permissions information is available at www.nature.com/reprints.

Correspondence and requests for materials should be addressed to D.P.

Publisher's note: Springer Nature remains neutral with regard to jurisdictional claims in published maps and institutional affiliations.

Methods

PMN-xPT single crystals with nominal Ti concentrations $x = 0$, 20, 30, 35, 40, and 50 and with masses of 0.651 g (0PT), 1.02 g (20PT), 0.725 g (30PT), 0.136 g (35PT), 0.638 g (40PT), and 0.275 g (50PT) were tested for compositional stoichiometry via prompt gamma activation analysis on neutron guide NGD at the NIST Center for Neutron Research. Normalized to the number of moles of Pb, the measured Ti concentrations were $x = 0$, 21.7, 28.8, 33.0, 39.8 and 48.5.

Each crystal was measured on the neutron instrument Corelli[50,51] at the Spallation Neutron Source at Oak Ridge National Laboratory at about 6 K. Corelli employs a broad band of neutron energies between 10 meV and 200 meV to perform time-of-flight Laue diffraction and uses cross-correlation to provide elastic discrimination. Neutron data for the different crystals were normalized by mass so that the intensities can be directly compared to one another. Neutron events were placed in bins of size $0.02 \times 0.02 \times 0.02$ r.l.u. (where 1 r.l.u. $= 2\pi/d = 1.56$ Å^{-1}) using Mantid software[52,53] and were only symmetrized for Fig. 2. Fig. 2c, d, g and h were symmetrized using the full set of 48 cubic symmetry operations, while Fig. 2e and f were symmetrized by reflection across the $h = k$ plane; Fig. 2a and b were not symmetrized.

X-ray diffuse scattering measurements were performed on samples taken from the same $x = 0$ and x = 30 crystals that were studied on Corelli. The crystals were etched in a heated diluted HCl acid bath to ensure clean surfaces. Data were taken at CHESS beamline A2 using an incident beam energy of 56.7 keV and a Dectris Pilatus 6 M detector with a 1-mm-thick Si detector. The data were collected at 100 K, with samples cooled by flowing N_2 gas. During the measurements, the samples were continuously rotated in the beam at 1° per second over 370°, with images read out every 0.1 s. Three sets of rotation images were collected for each sample at each temperature to fill in gaps between the detector chips. The resulting images were stacked into a three-dimensional array, oriented using an automated peak search algorithm, and transformed in reciprocal space coordinates using the software package CCTW (Crystal Coordinate Transformation Workflow)[54]. A significant Compton scattering artifact in the Si detector was observed around strong Bragg reflections; pixels affected by this artefact have been removed from Fig. 3.

Data availability. The experimental data that support the findings of this study are available from the corresponding author upon request.

References

50. Rosenkranz, S. & Osborn, R. Corelli: efficient single crystal diffraction with elastic discrimination. *Pramana J. Phys.* **71**, 705–711 (2008).
51. Ye, F., Liu, Y., Whitfield, R., Osborn, R. & Rosenkranz, S. Implementation of cross correlation for energy discrimination on the time-of-flight spectrometer CORELLI. *J. Appl. Cryst.* **51**, 315–322 (2018).
52. Arnold, O. et al. Mantid-data analysis and visualization package for neutron scattering and μ SR experiments. *Nucl. Instrum. Meth. Phys. Res. A* **764**, 156–166 (2014).
53. Michels-Clark, T. M., Savici, A. T., Lynch, V. E., Wang, X. & Hoffmann, C. M. Expanding Lorentz and spectrum corrections to large volumes of reciprocal space for single-crystal time-of-flight neutron diffraction. *J. Appl. Crystallogr.* **49**, 497–506 (2016).
54. Crystal Coordinate Transformation Workflow (CCTW). Advanced Photon Source, Argonne National Laboratory (2017); https://www.aps.anl.gov/Science/Scientific-Software/CCTW.
55. Singh, A., Pandey, D. & Zaharko, O. Powder neutron diffraction study of phase transitions in and a phase diagram of $(1-x)[Pb(Mg_{1/3}Nb_{2/3})O_3]$-$xPbTiO_3$. *Phys. Rev. B* **74**, 024101 (2006).